Computational Materials Science 210 (2022) 111437

Contents lists available at ScienceDirect

Computational Materials Science

journal homepage: www.elsevier.com/locate/commatsci

Full Length Article

Conversion of stacking fault tetrahedra to bubbles in dual (Kr, He)-beam irradiated copper

Rayaprolu Goutham Sreekar Annadanam [a], Cuncai Fan [b,a], Tongjun Niu [a], Xinghang Zhang [a], Anter El-Azab [a,*]

[a] School of Materials Engineering, Purdue University, West Lafayette, IN 47907, USA
[b] Department of Mechanical Engineering, The University of Hong Kong, Pokfulam Rd, Hong Kong, China

ARTICLE INFO

Keywords:
Molecular dynamics
Stacking fault tetrahedra
Helium bubbles
Ion irradiation

ABSTRACT

Stacking fault tetrahedrons (SFTs) are commonly observed in irradiated face-centered-cubic metals with low-to-medium stacking fault energies. Several mechanisms were previously proposed for the removal of SFTs in irradiated solids, including high temperature annealing, interactions with interstitial atoms, dislocations, and twin boundaries, and transformation to dislocation loop under compressive stress. We propose a previously unreported mechanism for the removal of SFT in irradiated copper, supported by experiments and atomistic simulations. *In situ* experiments showed that helium bubble density increased at the expense of SFT density following the initial phase of dual 1 MeV Kr/12 keV He ion irradiation, suggesting a possible conversion of SFTs to helium bubbles. Atomistic simulations of the interactions of helium atoms with SFTs confirmed this possibility and revealed the collective effects of helium-induced shear stress that deformed the atomic planes of Cu leading to the destruction of the SFT and leaving behind helium atoms in vacancy clusters (bubbles).

1. Introduction

Stacking Fault Tetrahedrons (SFTs) are typical three-dimensional vacancy clusters observed in quenched, irradiated, or plastically deformed FCC metals with low stacking fault energies [1–10]. SFTs also formed in aluminum which has high stacking fault energy due to interaction with high energy particles [11]. SFTs have stacking faults on each of their four faces with stair rod dislocations as their edges resulting from a certain "collapse" of a frank loop. As SFTs can significantly affect the mechanical and radiation resistance of metallic materials [12–15], extensive research has been performed to understand the formation mechanisms of SFTs in metals. A well-known SFT formation mechanism from Frank dislocation loops, collapsed vacancy clusters, is the Silcox-Hirsch mechanism [6], whereby Frank partials dissociate into stair-rod dislocation and Shockley partials, followed by the glide of Shockley partials along the close-packed planes of FCC metals, creating stacking faults on the SFT faces. Alternative SFT formation mechanisms involve the direct transformation from voids [16,17], vacancy cluster diffusion and aggregation [18], cross-slip of partial dislocations [19], and the annihilation of edge dislocation dipoles [20]. Until recently, SFTs were identified as sessile defects; however, molecular dynamics simulations showed small SFTs constituted of less than 21 vacancies could migrate at diffusivities of magnitude three-orders larger than vacancy diffusivity at low temperatures [21]. The latter discovery led to another mechanism for SFT growth, apart from the vacancy absorption and growth through ledge mechanism [22], wherein the small SFTs migrate and combine [21]. SFTs can be annihilated through various mechanisms: high-temperature annealing; interaction with self-interstitial atoms (SIAs) [23], mobile dislocations [14,24,25], and coherent twin boundaries in FCC metals [26]. Also, SFTs can collapse into Frank loops under compressive stresses [27].

It is well-known that helium impurities are common in materials in the nuclear fission and fusion environments [28]. High helium concentrations arise in these environments through their respective transmutation reactions [29]. Being insoluble in the solids, helium diffuses in the matrix and gets trapped at various trapping sites in the microstructure [28,30]. These trapping sites are commonly structural defects in the solid. For example, helium strongly binds with a vacancy to form a stable complex defect at a substitutional site in the lattice [31,32]. It accumulates in these sites forming tiny vacancy clusters, which could act as nucleation sites for voids [33] and He bubbles [34–36]. In the past, the dual-beam (heavy inert gas ion and helium) in situ studies focused primarily on bubble formation and its impact on the mechanical properties [37–39] and devoted less attention to its effects on the stability of SFTs.

* Corresponding author.

https://doi.org/10.1016/j.commatsci.2022.111437
Received 5 December 2021; Received in revised form 21 March 2022; Accepted 8 April 2022
Available online 18 April 2022

The strong bonding of helium atoms with vacancies forming the complex defects could explain the rare appearance of SFTs in the dual-beam irradiated samples. In the absence of helium, vacancy clusters could diffuse and aggregate to develop into SFTs, but the presence of helium prevents the vacancy clusters from transforming into SFTs, preferring to form bubbles. Nonetheless, it remains unclear how helium might interact with a pre-existing SFT formed by radiation damage.

Here, we report an atomistic study focusing on the helium interaction with an SFT in conjunction with single-beam and dual-beam in situ studies on copper (Cu) at 350 °C. We show that the presence of helium destabilizes SFTs and can completely remove them after reaching a certain concentration, leaving behind He clusters that can act as nuclei for bubble formation as suggested by the experimental observation. An examination of the energetics of the system showed the existence of a thermodynamic helium count on the faces of SFT, above which bubbles are energetically more stable than SFTs with helium on their faces, indicating the destabilizing effect that helium has over the SFT. Furthermore, we identified a favorable trajectory for the destabilization and removal of SFTs during their interaction with helium. These findings indicate an overlooked mechanism for the removal of SFTs via conversion into small helium/vacancy clusters (bubble nuclei).

2. Methodology

Pure (~99.95 wt%) copper (Cu) film, ~1 μm thick, was deposited on HF-etched Si (112) substrate using direct current magnetron sputtering technique at room temperature. After deposition, we analyzed the film texture by X-ray spectroscopy with a Cu Kα1 source. The XRD spectrum in Fig. S3(a) suggests the epitaxial growth of as-deposited film with Cu ⟨110⟩ // Si ⟨112⟩ along the growth direction. We fabricated plan-view TEM specimens from such Cu (110) film through polishing, dimpling, and low energy (3.5 keV) Ar ion milling. These specimens were subsequently irradiated by 1 MeV Kr^{++} and 12 keV He^{+} in the Intermediate Voltage Electron Microscope (IVEM) at Argonne National Laboratory, where an ion accelerator was attached to a Hitachi-9000 TEM operated at 200 kV. Before irradiations, we annealed the specimens at 350 °C for ~ 0.5 h. Fig. S3(b) represents a TEM micrograph for the annealed specimen that contains some growth dislocations and is oriented along with the Cu [011] zone axis, as demonstrated by the inset SAD pattern.

The specimen thickness is computed based on the convergent beam electron diffraction (CBED) technique [40]. The foil thickness ~ 130 nm was determined from the parallel Kossel-Mollenstedt (K-M) fringes taken under two-beam conditions with (022) strongly excited, as shown in Fig. S4(a) and Fig. S4(b). Fig. S4(c) schematically illustrates the experimental setup for in situ heavy-ion TEM irradiations; the ion beams, including 12 keV He^{+} and 1 MeV Kr^{++}, incident at ~ 30° from the electron beam and ~ 15° from the foil normal. We conducted two separate in-situ experiments to study the evolution of defects in pure Cu (110) films, both irradiated at 350 °C, one by a single beam of 1 MeV Kr^{++}, and the other by a dual beam of 12 keV He^{+} and 1 MeV Kr^{++}. In the single-beam irradiation, the specimen was irradiated by 1 MeV Kr^{++}; in the dual-beam irradiation, the specimen was irradiated simultaneously by 1 MeV Kr^{++} and 12 keV He^{+}. For Kr^{++} beam, the dose rate was controlled at ~ 6.3×10^{11} ions $cm^{-2}s^{-1}$ and to a fluence of 2×10^{14} ions cm^{-2}; for He^{+} beam, the dose rate was controlled at ~ 1.9×10^{12} ions $cm^{-2}s^{-1}$ and to a fluence of 6×10^{14} ions cm^{-2}. Fig. S4(d) and Fig. S4(e) show the depth profiles of ion concentration and radiation dose, calculated by using the Stopping and Range of Ions in Matter (SRIM) [41]. The calculations show that most of the high-energy Kr^{++} ions transmitted through the TEM foils and induced considerable damage, ~1.1 dpa on an average. By contrast, most low energy He^{+} ions stopped inside the foils and provided ~ 500 ppm (0.05 at. %) He in concentration. We also performed the post-irradiation analysis in FEI Talos 200X TEM.

We carried out the atomistic simulations using the LAMMPS Code [42]. We modeled the interactions between the copper atoms using the embedded atom method (EAM) potential [43] and the Cu-He and He-He interactions through Lennard-Jones (LJ) potential [44,45]. A comparative study is conducted, wherein we compared the results generated by the potential functions used in this work against the potential developed by Kashinath et al. [46]. The results show that the potentials used are adequately accurate (see Fig. S8). To model the helium effects on the SFT, we created a simulation cell of 30a × 75b × 45c, where a, b, and c refer to the lattice spacing along $[\bar{1}11]$, [110] and $[\bar{1}1\bar{2}]$, respectively, containing 607,500 atoms and employed periodic boundary conditions in the three orthogonal directions. We created SFTs of different sizes from the Frank loops by performing conjugate gradient energy minimization of the simulation cell. In this study, we studied six different SFTs with vacancy count in them being 28, 55, 78, 120, 171, and 231. Here, the size of SFT refers to the number of vacancies contained in the Frank loop that transformed into SFT. Later, we randomly distributed the helium atoms on the faces of SFT. We created bubbles of different sizes by scooping out atoms in a spherical shape and inserted helium into the voids. Conjugate gradient energy minimization is performed for all the configurations of bubbles and SFTs with helium. For simulating the dynamics at 623 K, we started by performing energy minimization of the cell for a few timesteps to adjust helium atom positions, followed by two stages of equilibration of the cell for about 50 ps at 623 K. During the equilibration of the cell, we controlled the temperature at 623 K and maintained the external pressure of the cell at zero using the Nose-Hoover thermostat and barostat (NPT ensemble). By setting the external pressure to zero, we allowed the simulation cell to relax, accommodating the inherent change in free volume due to the introduction of helium. Dynamic equilibrations took place in two stages. In the first, the helium atoms alone were relaxed for 0.5 ps. In the second, the whole system was equilibrated for 50 ps. The timesteps used in the two stages were 0.2 and 0.5 fs, respectively. To study the pressure map of the atoms in and around the SFT, we calculated the per-atom stress components of the Copper atoms. All post-processing and visualization were done in OVITO [47,48]

We used the NPT equilibrated defect structures to compute the free energy of the SFT and bubble configurations relative to a reference configuration in which the He atoms and vacancies are randomly distributed in the matrix. The Gibbs free energy change relative to the reference configuration, $\Delta G = \Delta U - T\Delta S$, was computed at a constant zero-pressure and temperature. Here, ΔU and ΔS are the changes in the internal energy (enthalpy at zero pressure) and entropy relative to the reference configuration. In our calculations, ΔU is found as an average over a sequence of configurations after equilibrium has been reached. We assume that entropy changes in going from the reference configuration to the SFT or bubble configurations have two contributions that can be assigned to Cu and helium atoms separately. Under isothermal scenarios, the entropy change of Cu atoms, ΔS_{Cu}, is related to the change in the volume occupied by the Cu atoms, ΔV_{Cu}, between the reference state and the SFT or bubble state, which is expressed in the form: $\Delta S_{Cu} = \alpha B \Delta V_{Cu}$ [49]. In the latter form, α is the volumetric coefficient of thermal expansion and B is the bulk modulus. The change in volume occupied by atoms, ΔV_{Cu}, at 623 K is calculated from the volume change at 0 K $\left(\Delta V_{Cu}^{0K}\right)$ through the relation $\Delta V_{Cu} = (1 + \alpha\Delta T)\Delta V_{Cu}^{0K}$. The quenched configuration of the NPT equilibrated structure is obtained by performing energy minimization under zero-pressure boundary condition. In this work, we considered $\alpha = 5.56 \times 10^{-5}$ K^{-1} and $B = 1.42 \times 10^{12}$ dyn cm^{-2} as reported in [16] at the zero temperature and zero pressure. The contribution from helium is approximated with a standard relation for the entropy change of an ideal gas at a constant temperature, which is $\Delta S_{He}^{1\to 2} = N_{He} k_B \ln\left(\frac{V_2}{V_1}\right)$, where N_{He} is the number of helium atoms, k_B is the Boltzmann constant, and V_1 and V_2 represent the volume occupied by the helium in the final and initial states, respectively. We assume that the volume occupied by helium atoms in the SFT and the random configurations to be the same, and equal to one atom volume of copper, Ω. In the bubble configuration, however, helium atoms occupy the volume

of the entire bubble. Therefore, $\Delta S_{He}^{SFT} = 0$ and $\Delta S_{He}^{Bubble} = N_{He} k_B \ln\left(\frac{V_{bubble}}{\Omega}\right)$. The free energies of the SFT and bubble structures relative to the random configuration are thus approximately determined up to the approximations made in the entropy part. A more accurate atomistic calculation of the free energies may be achieved using the histogram methods but they require time consuming MD simulations $(1-2\ \mu s)$ [50].

3. Results

3.1. Defect evolution in single-beam and dual-beam irradiation experiments at 623 K

The phenomenon of SFT annihilation upon helium irradiation was observed by two in-situ irradiation experiments (single-beam Kr^{++} radiation and dual-beam Kr^{++}, He^{+} irradiation) examining the evolution of defects in irradiated (pure) Cu (110) films. In-focus TEM micrographs in Fig. 1 show the formation of defect clusters in the single-beam irradiated (Fig. 1a-e) and dual-beam irradiated samples (Fig. 1f-j). The black spots in the micrographs represent the radiation-induced defect clusters. The presence of SFTs, the triangular-shaped defect clusters (Fig. 1c and Fig. 1h insets) and dislocation loops (Fig. 1h) was noted in both samples. In the dual-beam irradiated sample, bubbles form at a radiation dose of 0.25 dpa and around 125 ppm helium. An under-focus TEM micrograph revealed the nucleation and growth of bubbles with increasing helium concentration and radiation dose, as shown in Fig. 2. The post-irradiation analyses of the samples (Supplementary Fig. S1) confirmed that the single-beam and dual-beam irradiated samples contained primarily SFTs and helium bubbles, respectively.

Fig. 3 shows the density evolution of the defect clusters measured against radiation dose and helium concentration in single-beam and dual-beam irradiated samples. The defect evolution can be characterized into three stages. In a single-beam irradiated sample, a rapid rise in the densities of SFTs and loops occurs in stage I (0–0.1 dpa), saturating in stages II (0.1–0.3 dpa) and III [23]. In contrast, the densities of SFTs and loops increase rapidly in stage I during dual-beam irradiation but gradually decrease in stages II and III due to simultaneous formation of bubbles. Meanwhile, the density of bubbles rapidly grows in stage II while saturating in stage III. The increase in the bubble density at the cost of SFTs suggests that helium may be destabilizing the SFTs.

3.2. Relative thermodynamic stability of bubbles and SFTs with helium at 623 K

Comparing the free energies of configurations of helium in copper will allow us to examine regimes where the system may favor SFTs with helium over bubbles. In this regard, we compare the SFT and bubble configurations with the reference configuration mentioned earlier, which contain the same number of vacancies and He atoms. In the case of SFT, He atoms were randomly placed on one or all of its faces. The difference in free energy between the random configuration and either SFT or bubble configuration represents the amount of energy released via the clustering of point defects, which is referred to as the clustering free energy.

Fig. 4 and Supplementary Fig. S1 show the clustering free energy (normalized by the number of vacancies) for the SFT and bubble configurations. Fig. 4 reports the normalized clustering free energy for different SFT and bubble sizes containing varying numbers of helium atoms for the case where the helium atoms are distributed over more than one face of an SFT. In the absence of helium, SFT formation is energetically favorable over a void, in agreement with earlier studies [51]. For all SFT sizes studied, a helium count is observed above which bubbles are energetically more stable than SFTs. We refer to such a specific helium count as the "thermodynamic helium count." An increase in the number of helium atoms beyond the thermodynamic helium count increases the driving force for transforming SFT to bubbles (Fig. 4). The slope of the curves represents the increase in normalized clustering free energy per single helium atom added. This increase in clustering free energy is largely dependent on the distribution of helium on the faces.

In Supplementary Fig. S1, we reported the clustering free energy per vacancy of the defects when helium is distributed only on the $(\bar{1}11)$ plane of the SFTs. Note that the SFT clustering free energy curve differs from the case of Fig. 4 because of the initial distribution of helium atoms. Also, we reported the clustering energy of the defect structures at 0 K in Fig. S6 and Fig. S7 for the scenarios where helium is distributed over all faces and one face of SFT, respectively. The thermodynamic helium counts determined from the curves at 623 K and 0 K do not vary significantly as the internal energy largely influences it, but not the entropy. For the vacancy counts of SFTs studied in this work, we see that the initial distribution of helium has a weak influence over the thermodynamic helium count; however, a statistical analysis is required to accurately determine the influence of helium over the critical count. Furthermore, we define a quantitative measure called "thermodynamic

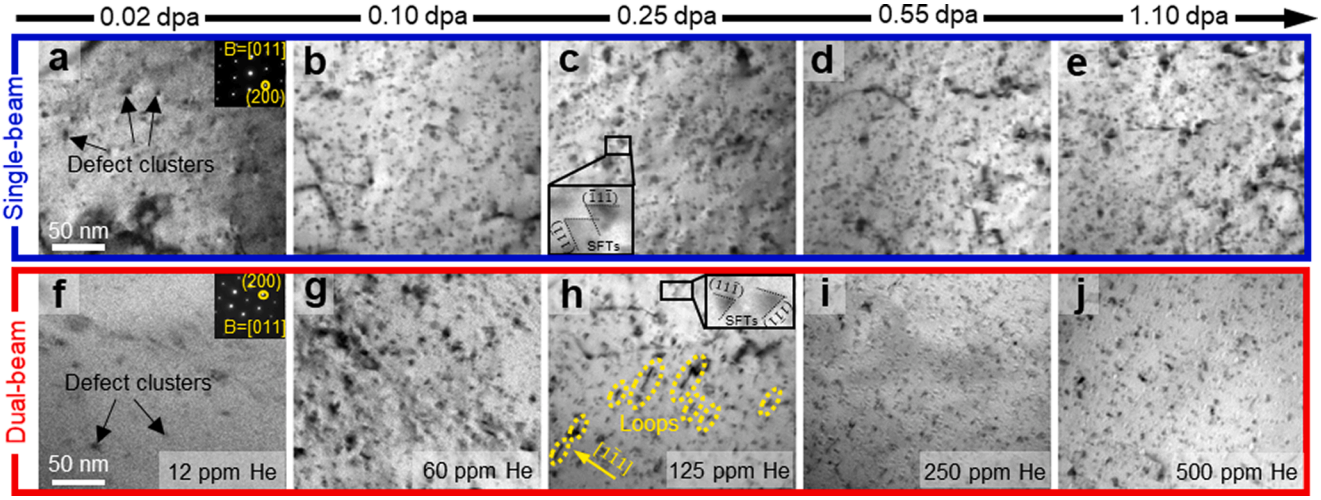

Fig. 1. Evolution of defect clusters in Kr single-beam and He+Kr dual-beam irradiated (110) single crystal Cu film at 623 K. (a-e) In-focus TEM micrographs examined along [011] zone axis showing the evolution of defect clusters with increasing dose in Kr ion single-beam irradiated samples. Abundant SFTs were observed in irradiated Cu as shown in (c). **(f-j)** The He+Kr dual-beam irradiation induces dislocation loops shown in (h) and He bubbles.

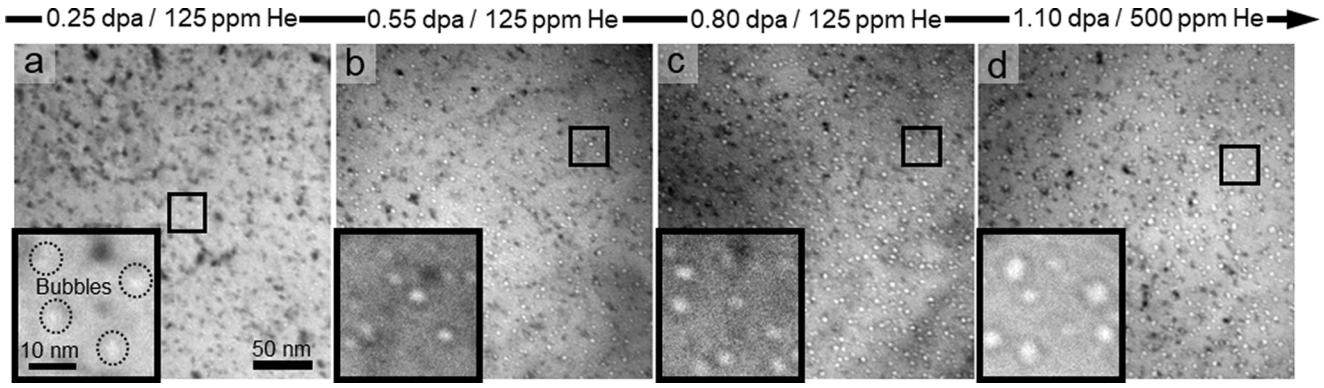

Fig. 2. Nucleation and growth of He bubbles. (**a-d**) Under-focus ($\Delta f \approx -1\mu m$) TEM micrographs of dual-beam irradiated sample from 0.25 to 1.10 dpa with the helium concentration varying from 125 ppm to 500 ppm. The inset boxes are the magnified views showing the nucleation and growth of He bubbles.

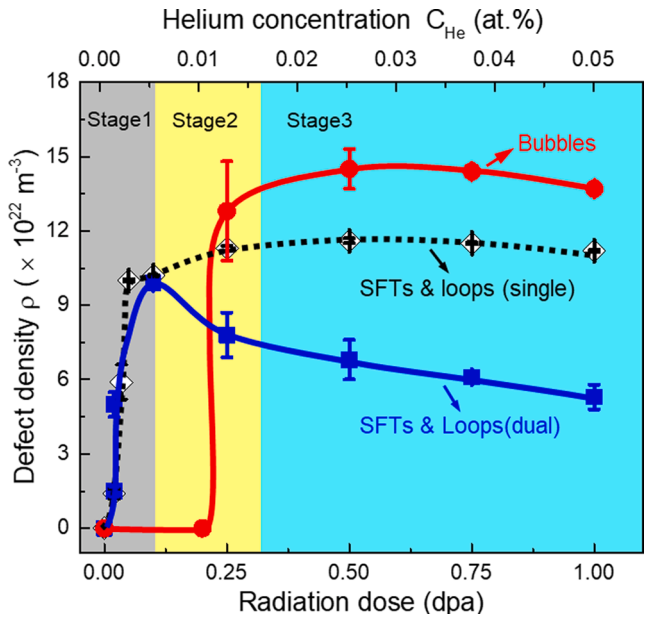

Fig. 3. Density evolution of defect clusters in single-beam and dual-beam irradiated Cu. For the single Kr ion beam irradiated Cu, the density of defect clusters (white diamonds) rises rapidly upon irradiation to 0.025 dpa and stays at a similar level in subsequent radiation. For the dual-beam irradiated samples, and density of SFTs and loops follow the similar path of single beam irradiation till 0.05 dpa, and then decreases gradually thereafter. Meanwhile, the density of Helium bubbles (red spheres) increases sharply when He concentration exceeds 0.01 at.% and reaches a plateau soon after.

helium efficacy" to capture the effectiveness of a single helium atom in destabilizing the SFT and is defined as the ratio of SFT vacancy count and thermodynamic helium count. In Fig. 5, we reported the thermodynamic helium efficacy as a function of the SFT size for the case when helium is distributed on one or all faces. The thermodynamic helium efficacy improves with the size of the SFT, suggesting an increasing effectiveness of helium atom in destabilizing the SFT at 623 K.

3.3. Dynamics of SFT with helium at 623 K

A confirmation of the findings of the above thermodynamic studies can be obtained using molecular dynamics (MD), where the entropic effects are naturally accounted. Fig. 6 shows the configurations of SFTs consisting of 78 and 231 vacancies with the increase in helium on their $(\bar{1}11)$ plane. It is clear from Fig. 6 that SFT size shrinks as the helium count increases on the face. The reduction in SFT size occurs gradually till the helium count on the face reaches a dynamic helium count. At the dynamic-helium count (which is significantly higher than the thermodynamic helium count), there is total annihilation of the SFT. The presence of helium at the $(\bar{1}11)$ plane exerts pressure on the nearby copper atoms and displaces them away from the face. We showed the displaced atoms in golden-yellow spheres in Fig. 6a-d and Fig. 6f-i. The number of displaced atoms increases with helium count and reaches a maximum at the total annihilation of SFT. Also, the shrinkage in SFT size directly correlates with the number of displaced atoms (Fig. 6). Moreover, helium atoms at the base of the SFT diffuse to form small clusters, which act as the nuclei for bubble formation. We show one such formation for the case of dynamic-helium count (Fig. 6e and Fig. 6j). These helium clusters are also observed when the helium count is less than the critical value, and they co-existed alongside truncated SFT (Fig. 6a-d and Fig. 6f-i).

Fig. 7 shows a detailed examination of the annihilation mechanism of an SFT containing 78 vacancies for a helium count of fifty-five, although this mechanism applies to all the other sizes of SFT at or greater than the critical value of helium. The SFT removal originates at the site of helium atoms and proceeds towards the apex, opposite to the face containing helium (Supplementary movie M1). Helium is an inert element and therefore possesses a stable electron configuration. As a result, helium repels nearby copper atoms. Due to the prohibitively long timescales involved, we do not let the helium atoms diffuse to the surfaces of SFT; instead, we place them directly on the face. As the dynamics begin, the helium pushes all the nearby copper atoms away from itself (Fig. 7b). The atoms moving into the SFT displace the adjacent Cu layers, and in turn, they displace other adjacent planes of atoms, eventually removing the SFT. The atoms displaced towards the SFT get accommodated because it is a vacancy-type defect cluster, whereas the copper atoms displaced away from the SFT are pushed back by the bulk atoms and thus settling back in their original positions (Fig. 7e-f). Like the thermodynamic helium efficacy, we define a dynamic-helium efficacy that quantifies the effectiveness of single helium in totally removing the SFT. In Fig. 9, alongside the thermodynamic helium efficacy, we also reported the "dynamic helium efficacy" in the case when helium is distributed on only $(\bar{1}11)$ plane. The dynamic-helium efficacy is the ratio of the SFT vacancy count and the dynamic-helium count. Unlike thermodynamic helium efficacy, dynamic-helium efficacy decreases with the size of SFTs.

To study the influence of the spatial distribution of helium on the stability of SFT structure, we examined dynamics on configurations where the helium was distributed on multiple faces. For example, Fig. 8 shows the SFT containing 78 vacancies with 55 helium atoms distributed over two faces after running the dynamics for 50 ps, as shown in Fig. 8a. The equilibrated structure contains a remnant of SFT left behind. Note that the same 55 helium atoms completely removed the SFT when all helium atoms existed on one face. Helium's presence on both faces

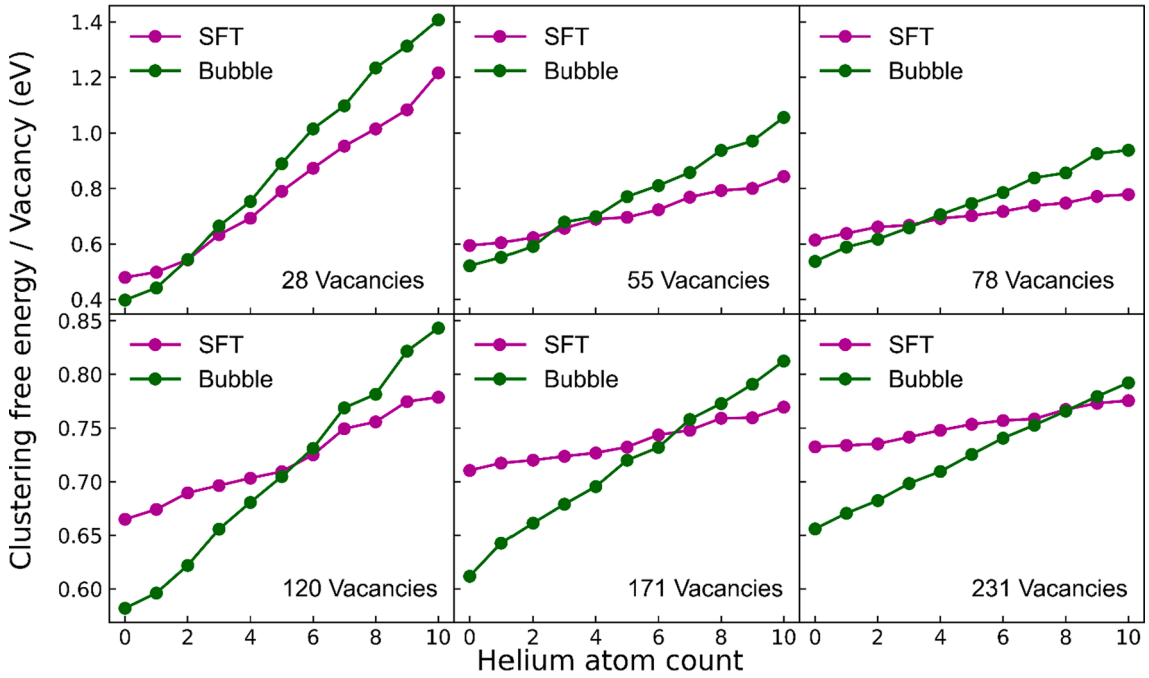

Fig. 4. Thermodynamic stability of SFTs and He bubbles when helium is distributed randomly on all SFT faces at 623 K. The simulations show the existence of critical helium count beyond which bubbles become relatively more stable than SFTs.

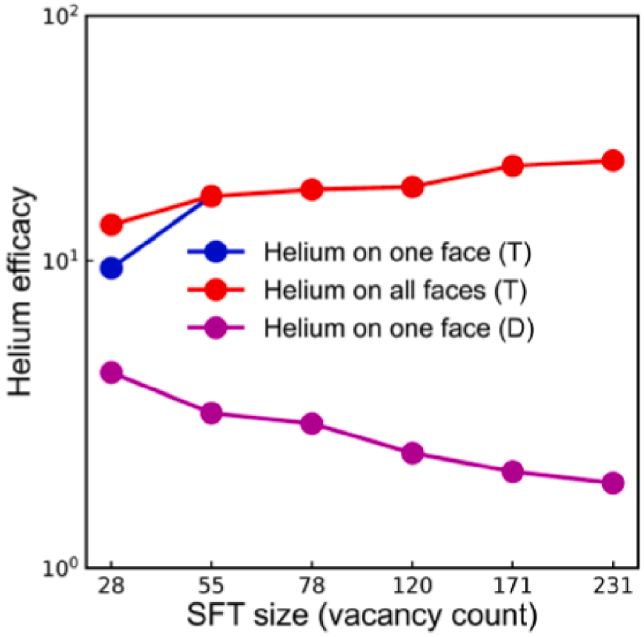

Fig. 5. Comparison of helium efficacy obtained from thermodynamics (T) and dynamics (D) results. Here, helium efficacy is a function of SFT size and measures the effectiveness of a single helium atom in destabilizing/annihilating an SFT. Note that the blue and red curves overlap beyond the vacancy count 28.

resulted in the displacement of copper atoms towards all the vertices of the SFT (Fig. 8b-d). Therefore, a lack in the coordinated motion of the copper atoms towards any vertex resulted in an unperturbed region where the remnant SFT resides.

4. Discussion

SFTs are vacancy defect clusters, and their continuous production occurs in the Cu (110) film due to heavy-ion bombardment. As mentioned earlier, they can get annihilated by absorption of self-interstitial atoms (SIAs) [23]. Nonetheless, the effect of SIAs on SFTs during irradiation appears to be minimal. Based on the post-irradiation analysis (Supplementary Fig. S2), the SFTs are around 3.5±1.1 nm in edge length and are composed approximately of 78 vacancies on an average. The post-irradiation analysis of single-beam irradiated samples in single-crystalline Cu revealed primarily the presence of SFTs, confirming that a considerable amount of SIAs annihilated at the surface of the films [52]. Therefore, the density profile of defects (Fig. 3) provides evidence for the reduction in density of SFTs primarily due to the interaction of helium but not because of SIA interaction with SFTs.

The mechanism reported in this study is distinctly different from that of the inverse Silcox-Hirsch mechanism. The Silcox-Hirsch mechanism [6] can be described in terms of the motion of atoms during the SFT formation process. The formation of SFTs involves layers of atoms present in the planes above the triangular Frank loop dropping down into the empty region of the loop. On average, the atoms in the SFT move ~ 1.59 Å (one Burgers vector of the partial dislocation). Here, we considered an extreme case where all helium atoms approached the SFT through one of its faces, and the annihilation of SFT originated at the base of SFT. In an inverse Silcox-Hirsch mechanism, the removal of SFT should start from one of the vertices of the SFT. The atoms at the vertex would get displaced first, followed by the atoms in the successive layers. However, in the mechanism we report, the annihilation originates from one of the faces of SFT and proceeds towards the vertex opposite to the face, which is a novel mechanism for the removal of SFTs in FCC metals. Also, the SFT removal mechanism in the case of multi-face helium distribution is apparent from Fig. 8. In the latter case, annihilation occurs when all the copper atoms move towards the nearest vertex of the SFT.

In the simulations, we placed helium directly on the SFTs to study both the thermodynamics and dynamics of SFTs. We did so to avoid simulating the diffusion of helium towards SFT because of the prohibitive timescales associated and the irrelevance to the problem at hand, which is to determine the SFT removal mechanism. A helium atom could occupy different locations on SFT: faces, edges, and vertices of the SFTs. Depending on the concentration of helium in the copper, it could prefer either tetrahedral or octahedral sites [32]. However, in this study, we

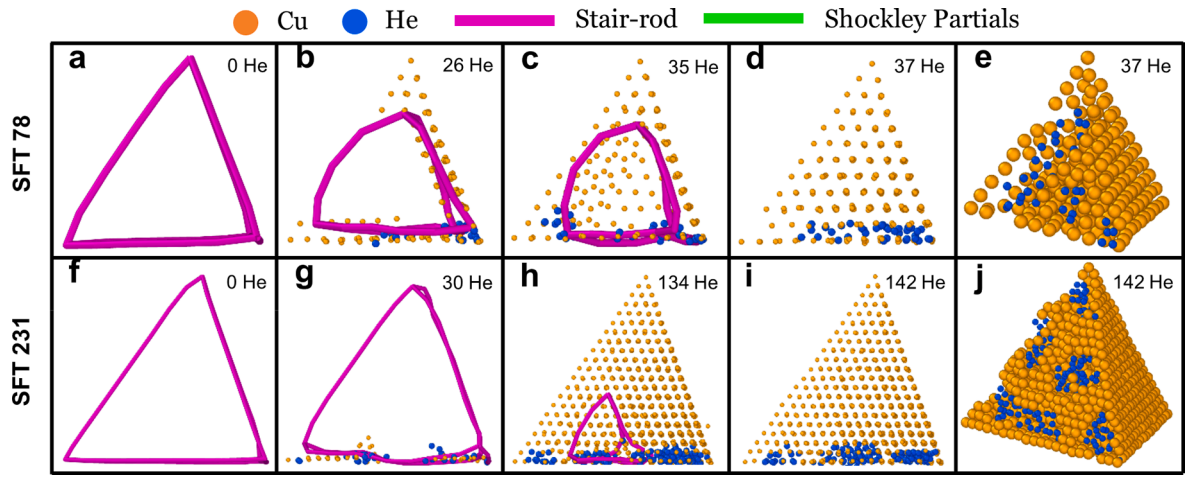

Fig. 6. Impact of helium on the stability of an SFT. Equilibrated structures of SFT with helium, placed randomly on only one face, at 623 K after 50 ps. The schematics depict the shrinkage and removal of (a-d) an SFT with 78 vacancies and (**f-i**) SFT-231 with an increase in helium count. (**e, j**) Helium clusters act as nuclei for bubble growth on the $(\bar{1}11)$ face of the SFT. The copper atoms shown in (**a-j**) are displaced by 1–2 Å.

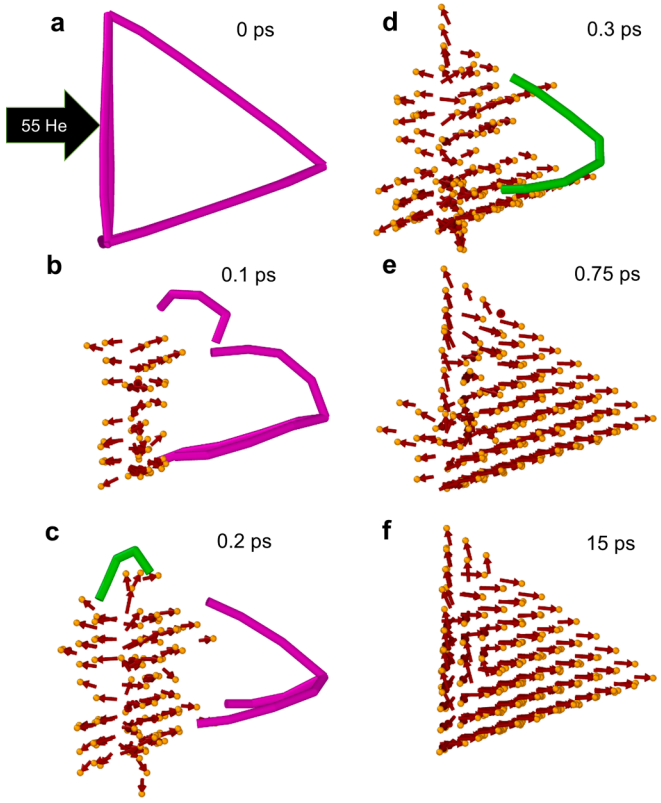

Fig. 7. Mechanism of SFT removal by He atoms. (**a-f**) Sequential snapshots of an SFT containing 78 vacancies with 55 helium atoms distributed on its face—marked by an arrow in (a)—revealing the SFT annihilation mechanism. The removal of the SFT originates at the site of helium atoms (**b**) and quickly progresses towards the apex (**c-f**), opposite to the face where helium resides. The arrows indicate the displacement vector of Cu atoms (colored in gold) of magnitude greater than 1 Å but less than 2 Å. The pink colored segments represent the stair-rod dislocations of a SFT, while the green colored segments in (**c, d**) are Shockley partials. Helium atoms are not shown for clarity.

placed the helium randomly in the interstices. The calculations of enthalpy of formation of helium in these sites will allow us to determine the most favorable locations among them. The enthalpy of formation of a helium defect contains not only the energy of the introduced helium atom, but also the work done against the environment to make space for its addition. As the internal energy of a helium atom is constant irrespective of where we place it on the SFT, the pressure map of the atoms in and around the SFT provides us with a qualitative understanding of the enthalpy of helium formation.

Fig. 9 shows the pressure map of the copper atoms in (Fig. 9a) and around (Fig. 9b) the SFT 231. We mapped out the pressure for only those atoms whose pressure is greater than 2200 MPa and smaller than −4000 MPa. Negative pressure implies atoms under tension. In SFT, atoms on the edges are under compression, while the rest are under tension. We can understand this variation in the pressure field by looking at the displacement of the atoms when a triangular Frank loop transforms into an SFT (Supplementary Fig. S5). The atoms surrounding the SFT see a vacant space in the SFT to occupy and move into the SFTs. The atoms move in such a way that they get squeezed on the edges of SFT (Supplementary Fig. S5a), and the maximum compression occurs at the center of the edge, as shown in Fig. 9b. Meanwhile, the atoms inside the SFT are under tension. As the layer of atoms above the Frank loop drop-in, they also simultaneously get stretched in the plane (Supplementary Fig. S5b). These planes of atoms stretch because they now enter a vacant triangular region bigger than themselves. The outer atoms above the faces are also under tension as they get pulled into the SFT space, as shown in Fig. 9b. Around vertices of SFT, the atoms are under tension but with a magnitude lower than 4000 MPa and hence not shown in Fig. 9b. Therefore, the enthalpy of helium formation is maximum on the edges because of compression and least on the faces as they are under tension.

The contrast between thermodynamic helium efficacy and dynamic-helium efficacy is evident because we computed the former from thermodynamics and the latter in dynamics. If looked at the extreme case where we place all the helium on the $(\bar{1}11)$ plane, beyond the thermodynamic helium count, SFT with helium is energetically unfavorable compared to the bubble, but it need not get annihilated when we run dynamics. The thermodynamics do not consider the work required to cross the migration barrier of all the copper atoms in the SFT. They only capture the energetics but not the kinetics of the transformation, thus explaining the apparent contrast between thermodynamics and dynamic simulation results. Moreover, unlike the thermodynamic helium count, it is difficult to determine the dynamic-helium count precisely. For example, in an SFT containing 78 vacancies, a helium count of 36 on the $(\bar{1}11)$ plane completely removed the SFT after running dynamics for 50 ps. However, at a helium count of 38, we observed a truncated SFT appear after 50 ps, and this appearance and disappearance of the SFT continued for other higher helium counts, and finally, the SFT gets

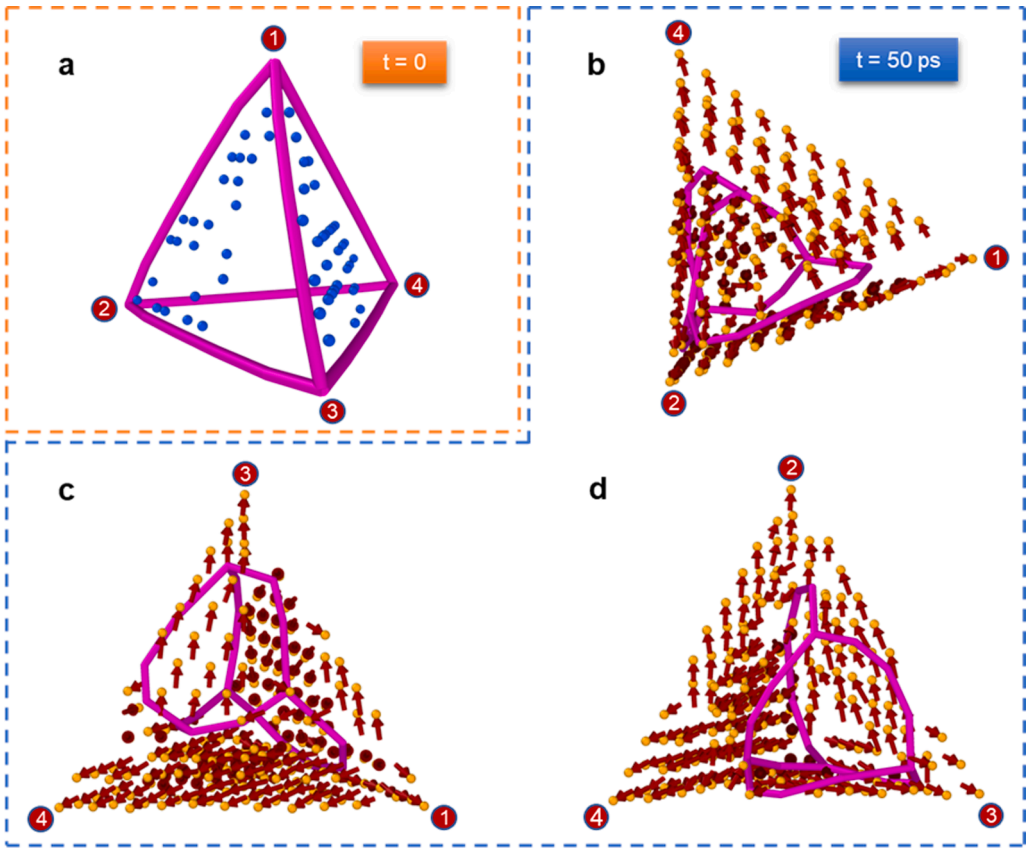

Fig. 8. Effect of spatial distribution of He on SFT stability at 623 K. (**a**) Initial distribution of 55 helium atoms on two different faces of an SFT-78. (**b-d**) Snapshots of the equilibrated structure, after 50 ps, taken at different orientations revealing the presence of remnant SFT and displacement of Cu atoms towards the four vertices. Helium on both faces of SFT has resulted in displacement of Cu atoms towards all the vertices of the SFT. The arrows indicate the displacement of Cu atoms.

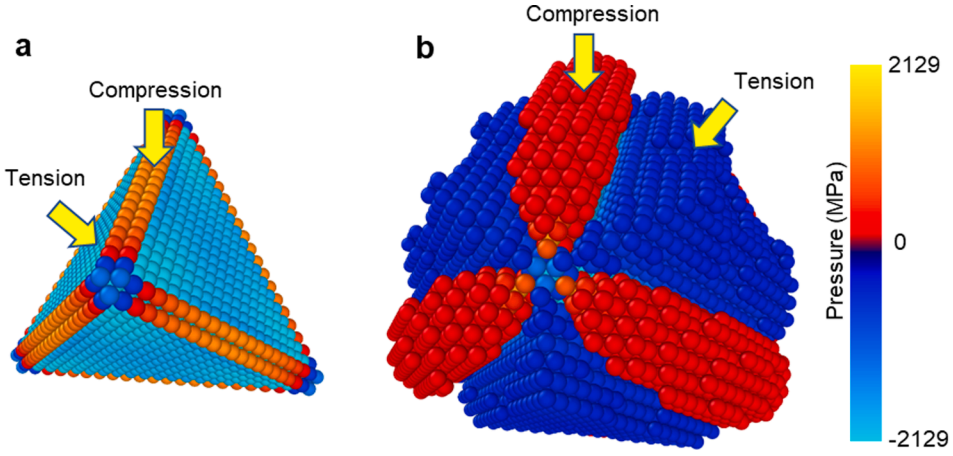

Fig. 9. Pressure map of atoms in and around an SFT with 231 vacancies. (**a**) Pressure map of atoms lying on SFT with compression on the edges and tension on the surfaces. (**b**) Pressure map of atoms around the SFT with compression around the edges and tension around the faces.

completely removed for helium counts above 47 (Supplementary movie M2). We chose the smallest helium count at which the SFT vanishes as the critical value. It is entirely possible to obtain a different dynamic-helium count for the SFTs when we sample different initial positions for the helium on the faces. In the case of multi-face helium distribution, determining the dynamic-helium count gets even more complicated because of the massive number of possibilities for selecting the helium atom's initial positions. Therefore, in this study, we did not attempt to compute the dynamic-helium counts for SFTs in the latter case.

Although this mechanism of SFT annihilation is probable in helium implanted thin films, its occurrence in the bulk material could be surprisingly low. Typically, helium production in these materials occurs through transmutation reactions. The helium then must diffuse in the bulk to approach the SFTs. However, point defects and other defects produced in the irradiation environment could trap the helium and prevent it from approaching the SFT. In the thin-film implantation process, we provide helium with sufficient kinetic energy that could direct it to the faces of SFT and thus increasing the probability of noticing the mechanism reported in this study. In bulk samples, there exists a greater chance for SIAs to remove the SFTs because, unlike thin

films, there are not many sites available for SIAs to annihilate.

5. Conclusion

The transformation of the SFT to bubbles, under the presence of helium, has been systematically investigated using atomistic simulations. We present the following conclusions:

1. We observed that helium irradiation of Cu resulted in a reduction of SFT density after an initial rise, accompanied by a subsequent rise in the bubble density from in situ TEM experiments.
2. A thermodynamic helium count is observed in the atomistic simulations above which bubbles are energetically more stable than SFTs. An increase in helium count–beyond the thermodynamic helium count–increases the driving force for SFT transformation to bubbles. Also, a quantitative measure called thermodynamic helium efficacy is defined to capture the effectiveness of a single helium atom in destabilizing the SFT. The thermodynamic helium efficacy improves with the SFT size demonstrating the effectiveness of a single helium atom in destabilizing the SFT, which depends on the distribution of helium over its faces.
3. MD simulations confirmed the transition of SFTs to bubbles in the presence of helium. The SFT size shrinks gradually as the helium count is increased on the faces of SFT and gets annihilated when the count reaches the dynamic-helium count. Moreover, helium on the faces diffuses and forms clusters that act as the nuclei for the bubble formation. Unlike thermodynamic helium efficacy, dynamic-helium efficacy decreases with the size of SFTs because thermodynamic simulations do not consider the work required to cross the migration barrier of all the copper atoms in the SFT. The thermodynamic simulations only capture the energetics but not the kinetics of the transformation process, thus explaining the apparent contrast between thermodynamics and dynamic simulation results.
4. Our simulations revealed a novel mechanism for the SFT removal, whereby the helium atoms displace the Cu atoms towards any of the vertices of the SFT and the count at which the SFT annihilates depends highly on the spatial distribution of helium on the faces.
5. The simulations also revealed a favorable trajectory for the helium atoms to diffuse towards the SFT. The pressure map of the atoms qualitatively provided us with information regarding the formation energy of helium atom, revealing that the helium would prefer to diffuse more towards the faces of the SFTs than towards edges or corners of the SFT.

CRediT authorship contribution statement

Rayaprolu Goutham Sreekar Annadanam: Formal analysis, Investigation, Methodology, Visualization, Writing – original draft. **Cuncai Fan:** Conceptualization, Investigation, Methodology, Data curation, Visualization, Writing – review & editing. **Tongjun Niu:** Investigation, Writing – review & editing. **Xinghang Zhang:** Conceptualization, Funding acquisition, Writing – review & editing. **Anter El-Azab:** Methodology, Resources, Funding acquisition, Writing – review & editing.

Declaration of Competing Interest

The authors declare that they have no known competing financial interests or personal relationships that could have appeared to influence the work reported in this paper.

Acknowledgements

We acknowledge the financial support by NSF-CMMI-1728419. We would also like to acknowledge Joseph Anderson and Ahmad Ahmad for their critical review of the manuscript.

Data availability

All data generated and/or analyzed in this study are included in the article and its Supplementary information file. The raw simulation data and other datasets are available from the author on reasonable request.

Appendix A. Supplementary data

Supplementary data to this article can be found online at https://doi.org/10.1016/j.commatsci.2022.111437.

References

[1] M. Kiritani, Story of stacking fault tetrahedra, Mater. Chem. Phys. 50 (2) (1997) 133–138, https://doi.org/10.1016/S0254-0584(97)80250-7.
[2] M.H. Loretto, P.J. Phillips, M.J. Mills, Stacking fault tetrahedra in metals, Scr. Mater. 94 (2015) 1–4, https://doi.org/10.1016/j.scriptamat.2014.07.020.
[3] R. Schäublin, Z. Yao, N. Baluc, M. Victoria, Irradiation-induced stacking fault tetrahedra in fcc metals, Phil. Mag. 85 (4-7) (2005) 769–777, https://doi.org/10.1080/14786430412331319929.
[4] K. Nordlund, F. Gao, Formation of stacking-fault tetrahedra in collision cascades, Appl. Phys. Lett. 74 (18) (1999) 2720–2722, https://doi.org/10.1063/1.123948.
[5] S. Crampin, K. Hampel, D.D. Vvedensky, J.M. MacLaren, The Calculation of Stacking Fault Energies in Close-Packed Metals, J. Mater. Res. 5 (10) (1990) 2107–2119, https://doi.org/10.1557/JMR.1990.2107.
[6] J. Silcox, P.B. Hirsch, Direct observations of defects in quenched gold, 8086 (2006). 10.1080/14786435908238228.
[7] C. Fan, A.R.G. Sreekar, Z. Shang, J. Li, M. Li, H. Wang, A. El-Azab, X. Zhang, Radiation induced nanovoid shrinkage in Cu at room temperature: An in situ study, Scr. Mater. 166 (2019) 112–116, https://doi.org/10.1016/j.scriptamat.2019.02.046.
[8] Y. Chen, J. Li, K.Y. Yu, H. Wang, M.A. Kirk, M. Li, X. Zhang, In situ studies on radiation tolerance of nanotwinned Cu, Acta Mater. (2016), https://doi.org/10.1016/j.actamat.2016.03.039.
[9] S.J. Zinkle, Microstructure and properties of copper alloys following 14-mev neutron irradiation, J. Nucl. Mater. 150 (2) (1987) 140–158, https://doi.org/10.1016/0022-3115(87)90070-5.
[10] X. Zhang, K. Hattar, Y. Chen, L. Shao, J. Li, C. Sun, K. Yu, N. Li, M.L. Taheri, H. Wang, J. Wang, M. Nastasi, Radiation damage in nanostructured materials, Prog. Mater Sci. 96 (2018) 217–321, https://doi.org/10.1016/j.pmatsci.2018.03.002.
[11] Y. Satoh, T. Yoshiie, H. Mori, M. Kiritani, Formation of stacking-fault tetrahedra in aluminum irradiated with high-energy particles at low-temperatures, Phys. Rev. B - Condensed Matter and Mater. Phys. 69 (2004) 1–11, https://doi.org/10.1103/PhysRevB.69.094108.
[12] H.-J. Lee, B.D. Wirth, Molecular dynamics simulation of the interaction between a mixed dislocation and a stacking fault tetrahedron, Phil. Mag. 89 (9) (2009) 821–841, https://doi.org/10.1080/14786430902776954.
[13] M. Victoria, N. Baluc, C. Bailat, Y. Dai, M.I. Luppo, R. Schaaublin, B.N. Singh, The microstructure and associated tensile properties of irradiated fcc and bcc metals, J. Nucl. Mater. 276 (1-3) (2000) 114–122, https://doi.org/10.1016/S0022-3115(99)00203-2.
[14] M. Niewczas, R.G. Hoagland, Molecular dynamics studies of the interaction of a/6 h112i Shockley dislocations with stacking fault tetrahedra in copper. Part I: Intersection of SFT by an isolated Shockley, Philos. Mag. 89 (2009) 623–640, https://doi.org/10.1080/14786430902740737.
[15] N. Nita, R. Schaeublin, M. Victoria, R.Z. Valiev, Effects of irradiation on the microstructure and mechanical properties of nanostructured materials, Phil. Mag. 85 (4-7) (2005) 723–735, https://doi.org/10.1080/14786430412331319965.
[16] B.P. Uberuaga, R.G. Hoagland, A.F. Voter, S.M. Valone, Direct transformation of vacancy voids to stacking fault tetrahedra, Phys. Rev. Lett. 99 (2007) 1–4, https://doi.org/10.1103/PhysRevLett.99.135501.
[17] X.F. Kong, N. Gao, I.J. Beyerlein, B.N. Yao, S.J. Zheng, X.L. Ma, D. Legut, T. C. Germann, H.J. Zhang, R.F. Zhang, Interface facilitated transformation of voids directly into stacking fault tetrahedra, Acta Mater. 188 (2020) 623–634, https://doi.org/10.1016/j.actamat.2020.02.044.
[18] D.S. Aidhy, C. Lu, K. Jin, H. Bei, Y. Zhang, L. Wang, W.J. Weber, Formation and growth of stacking fault tetrahedra in Ni via vacancy aggregation mechanism, Scr. Mater. 114 (2016) 137–141, https://doi.org/10.1016/j.scriptamat.2015.12.020.
[19] J. Wei Wang, S. Narayanan, J. Yu Huang, Z. Zhang, T. Zhu, S.X. Mao, Atomic-scale dynamic process of deformation-induced stacking fault tetrahedra in gold nanocrystals, Nat. Commun. 4 (2013) 1–8, https://doi.org/10.1038/ncomms3340.
[20] H. Wang, D.S. Xu, R. Yang, P. Veyssire, The formation of stacking fault tetrahedra in Al and Cu: I. Dipole annihilation and the nucleation stage, Acta Materialia. 59 (2011) 1–9, https://doi.org/10.1016/j.actamat.2010.07.046.
[21] E. Martínez, B.P. Uberuaga, Mobility and coalescence of stacking fault tetrahedra in Cu, Sci. Rep. 5 (2015) 1–5, https://doi.org/10.1038/srep09084.
[22] H. Wang, D.S. Xu, R. Yang, P. Veyssire, The formation of stacking fault tetrahedra in Al and Cu: III. Growth by expanding ledges, Acta Materialia. 59 (2011) 19–29, https://doi.org/10.1016/j.actamat.2010.07.045.

[23] B.N. Singh, S.I. Golubov, H. Trinkaus, D.J. Edwards, M. Eldrup, Review: Evolution of stacking fault tetrahedra and its role in defect accumulation under cascade damage conditions, J. Nucl. Mater. 328 (2004) 77–87, https://doi.org/10.1016/j.jnucmat.2004.05.001.
[24] Y. Matsukawa, Y.N. Osetsky, R.E. Stoller, S.J. Zinkle, Mechanisms of stacking fault tetrahedra destruction by gliding dislocations in quenched gold, Phil. Mag. 88 (4) (2008) 581–597, https://doi.org/10.1080/14786430801898644.
[25] Y. Matsukawa, S.J. Zinkle, Dynamic observation of the collapse process of a stacking fault tetrahedron by moving dislocations, J. Nucl. Mater. 329–333 (2004) 919–923, https://doi.org/10.1016/j.jnucmat.2004.04.069.
[26] K.Y. Yu, D. Bufford, C. Sun, Y. Liu, H. Wang, M.A. Kirk, M. Li, X. Zhang, Removal of stacking-fault tetrahedra by twin boundaries in nanotwinned metals, Nat. Commun. 4 (2013) 1–7, https://doi.org/10.1038/ncomms2382.
[27] L. Zhang, C. Lu, G. Michal, G. Deng, K. Tieu, The formation and destruction of stacking fault tetrahedron in fcc metals: A molecular dynamics study, Scr. Mater. 136 (2017) 78–82, https://doi.org/10.1016/j.scriptamat.2017.04.019.
[28] Y. Dai, G.R. Odette, T. Yamamoto, The effects of helium in irradiated structural alloys, Elsevier Inc., 2012. 10.1016/B978-0-08-056033-5.00006-9.
[29] J. Knaster, A. Moeslang, T. Muroga, Materials research for fusion, Nat. Phys. 12 (5) (2016) 424–434.
[30] D.J. Reed, A review of recent theoretical developments in the understanding of the migration of helium in metals and its interaction with lattice defects, Radiation Effects. 31 (3) (1977) 129–147, https://doi.org/10.1080/00337577708233269.
[31] A.Y. Dunn, M.G. McPhie, L. Capolungo, E. Martinez, M. Cherkaoui, A rate theory study of helium bubble formation and retention in Cu–Nb nanocomposites, J. Nucl. Mater. 435 (1-3) (2013) 141–152.
[32] C. González, D. Fernández-Pello, M.A. Cerdeira, S.L. Palacios, R. Iglesias, Helium bubble clustering in copper from first principles, Modell. Simul. Mater. Sci. Eng. 22 (2014), https://doi.org/10.1088/0965-0393/22/3/035019.
[33] H. Wiedersich, B.O. Hall, Effect of mobile helium on void nucleation, J. Nucl. Mater. 66 (1-2) (1977) 187–192.
[34] C. Fan, Z. Shang, T. Niu, J. Li, H. Wang, X. Zhang, Dual Beam In Situ Radiation Studies of Nanocrystalline Cu, Materials. 12 (2019) 2721.
[35] W.G. Wolfer, Advances in void swelling and helium bubble physics, J. Nucl. Mater. 122 (1-3) (1984) 367–378, https://doi.org/10.1016/0022-3115(84)90626-3.
[36] W.G. Wolfer, Helium bubble formation and swelling in metals, J. Nucl. Mater. 104 (1981) 981–986.
[37] K.Y. Yu, Y. Liu, C. Sun, H. Wang, L. Shao, E.G. Fu, X. Zhang, Radiation damage in helium ion irradiated nanocrystalline Fe, J. Nucl. Mater. 425 (1-3) (2012) 140–146, https://doi.org/10.1016/j.jnucmat.2011.10.052.
[38] E.G. Fu, A. Misra, H. Wang, L. Shao, X. Zhang, Interface enabled defects reduction in helium ion irradiated Cu/V nanolayers, J. Nucl. Mater. 407 (3) (2010) 178–188, https://doi.org/10.1016/j.jnucmat.2010.10.011.
[39] J.A. Knapp, D.M. Follstaedt, S.M. Myers, Hardening by bubbles in He-implanted Ni, J. Appl. Phys. 103 (2008), https://doi.org/10.1063/1.2831205.
[40] D.B. Williams, C.B. Carter, The Transmission Electron Microscope BT - Transmission Electron Microscopy: A Textbook for Materials Science, in: D.B. Williams, C.B. Carter (Eds.), Springer US, Boston, MA, 1996: pp. 3–17. 10.1007/978-1-4757-2519-3_1.
[41] J.F. Ziegler, The stopping and ranges of ions in matter, Elsevier, 2013.
[42] S. Plimpton, Fast parallel algorithms for short-range molecular dynamics, J. Comput. Phys. 117 (1) (1995) 1–19.
[43] Y. Mishin, M.J. Mehl, D.A. Papaconstantopoulos, A.F. Voter, J.D. Kress, Structural stability and lattice defects in copper: Ab initio, tight-binding, and embedded-atom calculations, Phys. Rev. B - Condensed Matter and Mater. Phys. 63 (2001) 2241061–22410616, https://doi.org/10.1103/PhysRevB.63.224106.
[44] A. Neogi, H. Askari, N. Abdolrahim, Atomistic simulations of the strengthening effect of high-density bubble formation in helium irradiated single crystalline copper, Materialia. 1 (2018) 139–149, https://doi.org/10.1016/j.mtla.2018.04.004.
[45] W. Ling, N. Xi-Jing, Molecular dynamics simulations of helium behaviour in copper crystals, Chin. Phys. Lett. 20 (9) (2003) 1416–1419, https://doi.org/10.1088/0256-307X/20/9/302.
[46] A. Kashinath, M.J. Demkowicz, A predictive interatomic potential for He in Cu and Nb, Modell. Simul. Mater. Sci. Eng. 19 (2011), https://doi.org/10.1088/0965-0393/19/3/035007.
[47] A. Stukowski, Visualization and analysis of atomistic simulation data with OVITO–the Open Visualization Tool, Modell. Simul. Mater. Sci. Eng. 18 (2009) 15012.
[48] A. Stukowski, V. v Bulatov, A. Arsenlis, Automated identification and indexing of dislocations in crystal interfaces, Modelling and Simulation in Materials Science and Engineering. 20 (2012) 85007.
[49] R.D. Hatcher, R. Zeller, P.H. Dederichs, Formation entropy and the diffusion constant for vacancies in Cu and <span class, Phys. Rev. B. 19 (1979) 5083, https://doi.org/10.1103/PhysRevB.19.5083.
[50] D. Perez, L. Sandoval, B.P. Uberuaga, A.F. Voter, The thermodynamic and kinetic interactions of He interstitial clusters with bubbles in W, J. Appl. Phys. 119 (2016), https://doi.org/10.1063/1.4951706.
[51] S.J. Zinkle, L.E. Seitzman, W.G. Wolfer, S.J. Zinkle, W.G. Wolfer, I. Energy calculations for pure metals, Philos. Mag. A: Phys. Condensed Matter, Structure, Defects and Mech. Properties 55 (1987) 111–125, https://doi.org/10.1080/01418618708209803.
[52] C. Fan, R.G.S. Annadanam, Z. Shang, J. Li, M. Li, H. Wang, A. El-Azab, X. Zhang, Irradiation induced void spheroidization, shrinkage and migration in Cu at elevated temperatures: An in situ study, Acta Mater. 201 (2020) 504–516, https://doi.org/10.1016/j.actamat.2020.10.008.